Ultrasound in Med. & Biol., Vol. 40, No. 4, pp. 685–694, 2014

0301-5629/$ - see front matter

http://dx.doi.org/10.1016/j.ultrasmedbio.2013.05.019

● *Original Contribution for the Festschrift in honor of Robert C. Waag*

ELASTICITY ESTIMATES FROM IMAGES OF CRAWLING WAVES GENERATED BY MINIATURE SURFACE SOURCES

Alexander Partin,* Zaegyoo Hah,* Christopher T. Barry,† Deborah J. Rubens,‡ and Kevin J. Parker*

*Department of Electrical and Computer Engineering, University of Rochester, Rochester, New York, USA; †Department of Surgery, University of Rochester Medical Center, Rochester, New York, USA; and ‡Department of Radiology, University of Rochester Medical Center, Rochester, New York, USA

(*Received* 26 *February* 2013; *revised* 23 *May* 2013; *in final form* 24 *May* 2013)

Abstract—We describe a surface-based approach to the generation of shear wave interference patterns, called crawling waves (CrW), within a medium and derive local estimates of biomechanical properties of tissue. In previous experiments, elongated bars operating as vibration sources were used to generate CrW propagation in samples. In the present study, however, a pair of miniature circular vibration sources was applied to the overlying skin to generate the CrW within the medium. The shape and position of the miniature sources make this configuration more applicable for *in vivo* implementation. A modified ultrasound imaging system is used to display the CrW propagation. A shear speed mapping algorithm is developed using a detailed analysis of the CrW. The proposed setup is applied to several biomaterials including a homogeneous phantom, an inhomogeneous phantom and an *ex vivo* human liver. The data are analyzed using the mapping algorithm to reveal the biomechanical properties of the biomaterials. (E-mail: kevin.parker@rochester.edu) © **2014 World Federation for Ultrasound in Medicine & Biology.**

Key Words: **Crawling waves, Sonoelastography, Elasticity imaging, Local shear speed estimation, Shear waves.**

INTRODUCTION

Biomechanical properties of biologic soft tissues can serve as biomarkers of health or pathology (Hoyt et al. 2008b; Parker et al. 2011). In some diseases such as breast and prostate cancer, there are localized differences in stiffness and cancerous tumors are formed in softer healthy tissue. In other diseases such as liver fibrosis and liver cirrhosis, the overall stiffness of the organ itself is increased. Manual palpation has been commonly used by physicians to detect the presence of hard lesions within soft tissue. However, the limited accessibility of palpation and limited elastic contrast between the lesion and the background tissue typically encountered in clinical situations limit this qualitative approach.

Research studies in the area of elastographic imaging methods have been conducted for more than two decades. Elastography, which refers to the branch of non-invasive elasticity imaging, can be classified in terms of the imaging modality used to scan soft tissue and display the resulting elasticity maps. The commonly used modalities are ultrasound and magnetic resonance imaging (MRI) (Parker et al. 2011). In ultrasound elastography, methods can be divided with respect to the applied external excitation: vibration sonoelastography (Krouskop et al. 1987; Lerner and Parker 1987; Lerner et al. 1988; Yamakoshi et al. 1990), compression elastography (Ophir et al. 1991), vibrational transient elastography (Catheline et al. 1999; Sandrin et al. 2003) and acoustic radiation force techniques (Chen et al. 2007; Fatemi and Greenleaf 1998; Hah et al. 2012; Konofagou and Hynynen 2003; McAleavey and Menon 2007; Nightingale et al. 1999, 2001; Sarvazyan et al. 1998). Extensive reviews of the different techniques are available (Gao et al. 1996; Garra 2007; Greenleaf et al. 2003; Ophir et al. 1999; Parker et al. 2005, 2011; Sarvazyan et al. 1995). Sonoelastography is an ultrasound-based imaging technique that uses continuous harmonic vibrations and power Doppler scanning. It is a readily available, non-invasive, real-time imaging tool used in all experiments described in this article.

Address correspondence to: Kevin J. Parker, University of Rochester, Hopeman Building 203, PO Box 270126, Rochester, NY 14627–0126, USA. E-mail: kevin.parker@rochester.edu

Wu et al. (2004) used sonoelastography to image slowly propagating shear wave interference, crawling waves (CrW), generated by a pair of mechanical vibration sources. The sources, in the shape of elongated bars, were placed in close contact at opposite sides of the medium and oscillated along a direction parallel to the sides, as illustrated in Figure 1a (the pair of sources labeled *I*), thereby generating shear waves from each side of the medium. The ultrasound probe is placed at the same cross section with the vibration sources and displays the shear wave interference. When vibrations are applied with a slight offset between the vibration frequencies, the displayed interference would appear on the screen as slowly propagating stripes, hence the term *crawling waves*. The data were further analyzed to reveal the elastic properties of the medium. This method provided reliable *ex vivo* results (Barry et al. 2012; Castaneda et al. 2009), but is not well suited for *in vivo* use, mainly because of the location and size of the sources. Hoyt et al. (2008c) further suggested placing the bars and the ultrasound probe on the top surface to generate the CrW, as illustrated in Figure 1a (sources labeled *II*). Here, the bars vibrate in the direction normal to the surface. This setup was employed with *in vivo* skeletal muscle, and a previously developed algorithm (Hoyt et al. 2008a) was used to map the viscoelasticity of the muscle tissue. However, the algorithm used is valid only for a region of interest in which the CrW propagation pattern can be approximated as a planar propagation. Moreover, the size of the bars renders this setup unsuitable for *in vivo* use such as liver scanning.

In the work described in this article, a revised source configuration was introduced in which a pair of circular indenters with a small surface area are used as the vibration sources instead of the elongated bars, as illustrated in Figure 1b. The location and dimensions of the sources make this elasticity mapping method a more applicable approach to *in vivo* scanning. The theory behind this configuration is described, and detailed explanations are provided for: the sonoelastography imaging mode that is used to detect and display the wave propagation within the medium; the vibration source configuration used to generate shear wave propagation using both one and two vibration sources; and the algorithm for mapping the elastic properties within the medium. Detailed analysis of the displacement field is presented, and consequently, the estimation algorithm, which is valid for the entire scanned region of interest, is developed. Experiments and results for a homogeneous phantom, an inhomogeneous phantom and an *ex vivo* human liver are described to examine the performance of the suggested method.

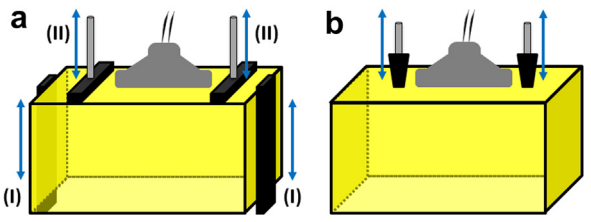

Fig. 1. Vibration setups used in previous (a) and current (b) studies. Previously, elongated bars were used to generate the crawling waves (CrW) by vibrating the sides (sources labeled *I*) or the top (sources labeled *II*) of the medium. In this study, the sources with a small circular surface area vibrate on top of the medium surface to generate the CrW propagation as shown in (b).

THEORY

Elasticity theory

The stiffness of soft tissues can be quantitatively expressed in terms of shear modulus (in pascals). In a linear, isotropic and elastic medium, the relationship between the shear modulus G, shear speed c_s, mass density ρ, angular frequency of the shear wave ω and shear wavenumber k_s, is

$$c_s = \sqrt{\frac{G}{\rho}} = \frac{\omega}{k_s} \tag{1}$$

It is acceptable to represent stiffness using only the shear speed value because the mass density of most soft tissues is nearly 1 g/cm^3. A quantitative elasticity map is advantageous over the qualitative result, especially in liver fibrosis and liver cirrhosis, where the average stiffness of the liver on an absolute scale is desired. All the results in this article are expressed in the form of shear speed maps.

Sonoelastography imaging

Sonoelastography is an ultrasound-based imaging technique in which external continuous harmonic vibrations excite the tissue to generate shear waves within the desired organ. The tissue scatterers oscillate in a sinusoidal fashion around their equilibrium position as the harmonic wave propagates. Compared with relatively soft tissues, regions of high stiffness will respond with lower displacement (Lerner et al. 1990). Doppler scanning is used to detect displacements of vibrating scatterers. The power spectrum spread of the backscattered echo from a vibrating scatterer is linearly proportional to the displacement amplitude of the vibration (Huang et al. 1990) and is given by

$$\sigma = \frac{\sqrt{2}\omega_0\omega}{c} \cdot u \tag{2}$$

where σ is the spread (standard deviation) of the Doppler power spectrum, u is the displacement amplitude, ω_0 is

the angular frequency of the insonifying ultrasound wave, ω is the angular frequency of the vibration source and c is the compressional speed of sound. Sonoelastography employs a real-time computation of spectral variance to represent the intensity of the local particle displacement. The variance of the power spectrum, derived by Kasai et al. (1985), is computed with

$$\sigma^2 = \frac{2}{T_{\mathrm{PRF}}}\left(1 - \frac{|R(T_{\mathrm{PRF}})|}{R(0)}\right) \tag{3}$$

where T_{PRF} is the time interval between successive ultrasound Doppler pulses, and R is the autocorrelation of the backscattered signals of a given Doppler packet. Local variance, corresponding to the local stiffness, is estimated using eqn (3) and displayed on the ultrasound screen in real time (Taylor et al. 2000). This variance image is called a *sonoelastogram.*

Vibration field from a circular load vibrating normal to the surface

To analyze the proposed double-source vibration setup in Figure 1b, a more fundamental configuration, in which only a single source is employed, is examined first. The geometry and coordinate system of the setup are illustrated in Figure 2a, and initially we consider only the left source (source 1) (the subscript 1 corresponding to source 1 is eliminated here for convenience, *e.g.*, $\omega_1 = \omega$). This source is positioned on top of the surface and vibrates with angular frequency ω in the direction normal to the surface (z axis), where A_s is the vibration amplitude, d is the lateral location of the source, r is the distance from the source and θ is the angle from the z axis. A rectilinear ultrasound transducer is placed on the same surface and scans the medium. Because the conventional Doppler system processes the axial component of the particle motions,

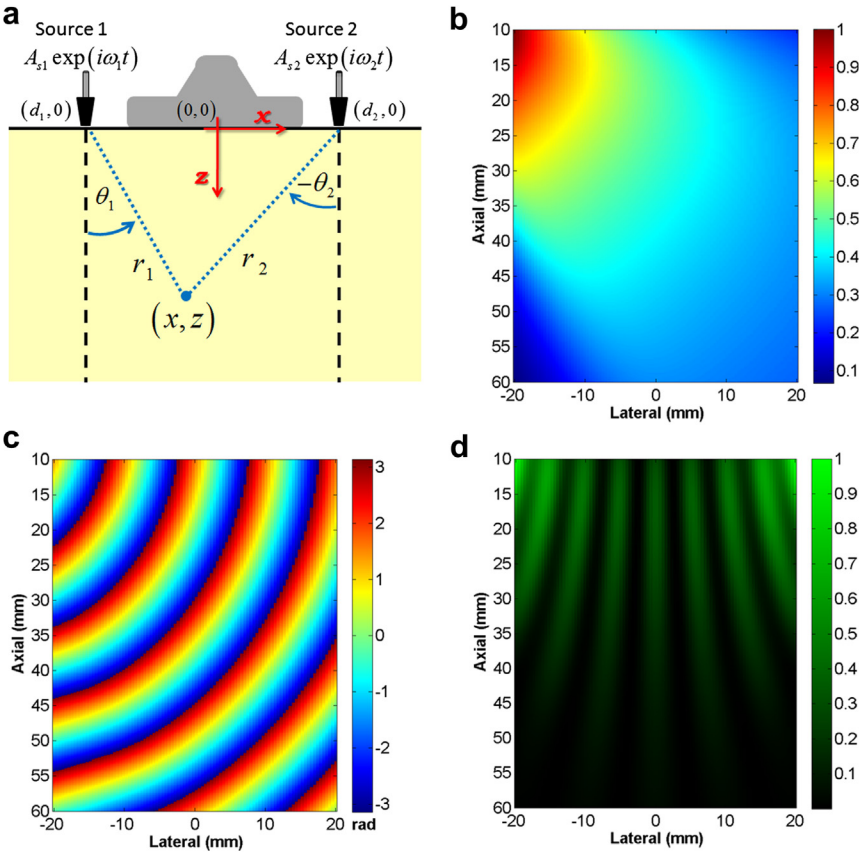

Fig. 2. Schematic and simulations of the vibration setups. (a) Two mechanical vibration sources shown in (a) generate shear wave interference within the medium *via* continuous harmonic vibrations in the direction normal to the surface of the medium. The sources and the ultrasound transducer define the imaging plane. The parameters ω, r, θ and d represent respectively the angular frequency of the vibrations, the distance from the source, the angle from the normal to the surface and the lateral location of the source. (b, c) The normalized magnitude (b) and the phase (c) of the axial displacement field generated by a single source (source 1) are illustrated using simulation and eqn (4). (d) A single frame of the simulated crawling waves movie (both sources vibrating). This image is the normalized square amplitude of the particle displacement. The shape and location of the stripes correspond to the mechanical properties of the medium.

only the z component of the displacement is of interest. According to Miller and Pursey (1954), the closed-form solution of the displacement field in the axial direction, valid in the far field, is

$$u_z = A_s \frac{ia^2\cos\theta}{2c_{44}k_c r}\cdot\left[\frac{2\mu^3\sin^2\theta\sqrt{\mu^2\sin^2\theta-1}}{F_0(\mu\sin\theta)}\cdot\exp(-ik_s r) + \frac{i\cos\theta(\mu^2-2\sin^2\theta)}{F_0(\sin\theta)}\cdot\exp(-ik_c r)\right]\exp(i\omega t) \quad (4)$$

where $i=\sqrt{-1}$, a is the radius of the circular load, c_{44} is the bulk modulus, k_c is the wavenumber of the compressional wave, k_s is the wavenumber of the shear wave, ω is the angular frequency of the shear wave, μ is the k_s/k_c ratio and $F_0(\zeta)$ is

$$F_0(\zeta) = \left(2\zeta^2-\mu^2\right)^2 - 4\zeta^2\sqrt{\left(\zeta^2-1\right)}\sqrt{\left(\zeta^2-\mu^2\right)} \quad (5)$$

$F_0(\zeta)$ is a complex function and thus can be expressed in the phasor form as

$$F_0(\zeta) = |F_0(\zeta)|\exp(i\gamma) \quad (6)$$

where

$$\gamma = \tan^{-1}\left\{\frac{\mathrm{Im}[F_0(\zeta)]}{\mathrm{Re}[F_0(\zeta)]}\right\} \quad (7)$$

The axial displacement field provided in eqn (4) consists of shear and compressional propagation components. The compressional propagation, however, can be neglected because the wavelength of the compressional wave is larger than human organs. This implies that the phase of the compressional wave is approximately constant over the scanned region of interest. We add an exponential attenuation term, α_s, for shear waves to account for loss in biologic tissues, and express the function F_0 in its phasor form; the displacement field can then be expressed as

$$u_z = \frac{A}{r}\exp(-\alpha_s r)\cdot\exp\left[i\left(\omega t - k_s r - \gamma + \frac{\pi}{2}\right)\right] \quad (8)$$

where A is a real number given by

$$A = A_s\frac{a^2\cos\theta}{2c_{44}k_c}\cdot\frac{2\mu^3\sin^2\theta\sqrt{\mu^2\sin^2\theta-1}}{|F_0(\mu\sin\theta)|} \quad (9)$$

Equations (8) and (9) describe a spherical wave with axial symmetry (Blackstock 2000), characterized by a geometric loss, where the field is inversely proportional to distance r. A simulation using eqn (8) is performed for a region of interest of 50 × 40 mm^2 with the parameters a = 0.5 cm, ρ = 1 g/cm^3, c_c = 1540 m/s, c_s = 3 m/s, f = 300 Hz, $k_c = 2\pi f/c_c$, $k_s = 2\pi f/c_s$, $c_{44} = \rho c_c^2$ and α_s = 0.25 Np/cm. The far-field distance in this case is $a^2/\lambda_s = a^2 f/c_s$ = 0.25 cm. The normalized magnitude and the phase from the simulation are illustrated in Figure 2 (b and c, respectively).

In the sonoelastography mode, where the square of the vibration amplitude is displayed, the displacement generated by a single vibration source is

$$|u_z|^2 = u_z\cdot u_z^* = \frac{A^2}{r^2}\exp(-2\alpha_s r). \quad (10)$$

As can be seen in eqn (10), the phase information that contains the shear speed is not displayed in sonoelastography when a single-source configuration is employed. To overcome this problem and increase the signal-to-noise ratio, the CrW technique is employed, where two sources are used to generate a slowly propagating interference of two shear waves. CrW excitation using a pair of normally vibrating sources is described in the next section.

Shear wave interference patterns

In the setup for generating CrW propagation with a pair of circular vibration sources, the ultrasound transducer is positioned between the vibration sources, and the center of the probe is defined as coordinate (0,0), as illustrated in Figure 2a. Two circular loads, vibrating normally to the surface, generate shear wave interference within the medium, where the subscripts 1 and 2 correspond to the left and right sources, respectively. The axial displacement of the interfering shear waves, u_T, is

$$u_T = u_{z1}+u_{z2} = \frac{A_1}{r_1}\exp(-\alpha_s r_1)\cdot\exp\left[i\left(\omega_1 t - k_{s1}r_1 - \gamma_1 + \frac{\pi}{2} + \phi_1\right)\right] + \frac{A_2}{r_2}\exp(-\alpha_s r_2)\cdot\exp\left[i\left(\omega_2 t - k_{s2}r_2 - \gamma_2 + \frac{\pi}{2} + \phi_2\right)\right] \quad (11)$$

where ϕ_1 and ϕ_2 are arbitrary phase terms. The squared amplitude of the displacement is

$$|u_T|^2 = u_T\cdot u_T^* = (u_{z1}+u_{z2})\cdot(u_{z1}+u_{z2})^* \quad (12)$$

By substituting eqn (11) into eqn (12), the interference pattern as displayed in the sonoelastogram is given by

$$|u_T|^2 = \frac{A_1^2}{r_1^2}\exp(-2\alpha_s r_1) + \frac{A_2^2}{r_2^2}\exp(-2\alpha_s r_2) + 2\frac{A_1A_2}{r_1r_2}\exp[-\alpha_s(r_1+r_2)]\cdot\cos[(\omega_1-\omega_2)t + k_{s2}r_2 - k_{s1}r_1 + (\gamma_2-\gamma_1) + (\phi_1-\phi_2)] \quad (13)$$

It is noted that the phase term containing the shear speed is preserved. The following notations are used to further simplify eqn (13):

$$\begin{aligned}\omega_1-\omega_2&=\Delta\omega\\ \gamma_2-\gamma_1&=\beta\\ \phi_1-\phi_2&=\phi_0\end{aligned}\tag{14}$$

$\Delta\omega$ is the difference between angular vibration frequencies, ϕ_0 is a constant phase term and β is a function of the coordinate system and the location of the vibration sources. The vibration sources are adjusted such that the difference between the frequencies is very small, that is, $\Delta\omega \ll \omega$. Accordingly, because $\Delta k_s = \Delta\omega/c_s \ll k_s$, then the shear wavenumbers of the propagating shear waves can be denoted as $k_{s1} \approx k_{s2} \approx k_s$. After the notations of eqn (14) and the condition $\Delta\omega \ll \omega$ are applied to eqn (13), the interference is

$$\begin{aligned}|u_T|^2=&\frac{A_1^2}{r_1^2}\exp(-2\alpha_s r_1)+\frac{A_2^2}{r_2^2}\exp(-2\alpha_s r_2)\\ &+2\frac{A_1A_2}{r_1r_2}\exp[-\alpha_s(r_1+r_2)]\\ &\cdot\cos[\Delta\omega t+k_s(r_2-r_1)+\beta(r_1-r_2)+\phi_0]\end{aligned}\tag{15}$$

The shear speed parameter k_s appears in the argument of the cosine term of eqn (15) and, therefore, can be estimated using an appropriate algorithm. A simulation using eqn (15) is performed for a region of interest of 50 × 40 mm^2 with the parameters a = 0.5 cm, ρ = 1 g/cm^3, c_c = 1540 m/s, c_s = 3 m/s, f_1 = 300 Hz, f_2 = 300.4 Hz, $k_c = 2\pi f/c_c$, $k_s = 2\pi f/c_s$, $c_{44} = \rho {c_c}^2$, α_s = 0.2 Np/cm, d_1 = 2 cm and d_2 = 2 cm. The normalized squared amplitude from the simulation is illustrated in Figure 2d. As can be seen, the CrW patterns are displayed in sonoelastography as curved stripes. The distance between the stripes and their shape correspond to mechanical properties of the medium at frequency 300 Hz. The argument of the cosine term in eqn (15) is further analyzed in the next section to develop the estimation algorithm that maps the local shear speed values in the region of interest.

Local shear speed estimation algorithm for elasticity mapping

The goal of the estimation algorithm is to estimate the local shear speed values within the scanned region of interest. After substitution of eqn (1) into eqn (15), the shear wave interference can be expressed by

$$|u_T|^2 = B+2\frac{A_1A_2}{r_1r_2}\exp[-\alpha_s(r_1+r_2)]\cdot\cos[\Delta\omega t+\varphi(c_s,r)]$$

$$\varphi(c_s,r)=\frac{\omega}{c_s}(r_2-r_1)+\beta(r_1,r_2)+\phi_0\tag{16}$$

where $\varphi(c_s, r)$ denotes the spatial phase term of the interference, and B is the baseline term. The rectilinear ultrasound probe, used in this study, provides the data in Cartesian coordinates. After appropriate coordinate transformations (polar to Cartesian) are applied to the spatial variables r_1 and r_2, the spatial phase $\varphi(c_s, r)$ is

$$\begin{aligned}\varphi(c_s,x,z)=&\frac{\omega}{c_s}\left(\sqrt{(x-d_2)^2+z^2}-\sqrt{(x-d_1)^2+z^2}\right)\\ &+\beta(x,z)+\phi_0\end{aligned}\tag{17}$$

By computing the gradient of $\varphi(c_s, x, z)$ in the x direction, the local shear speed estimate $\hat{c}_s(x,z)$ can be extracted with

$$\begin{aligned}\hat{c}_s(x,z)=&\omega\left(\frac{\partial\varphi}{\partial x}-\frac{\partial\beta}{\partial x}\right)^{-1}\\ &\times\left(\frac{x-d_2}{\sqrt{(x-d_2)^2+z^2}}-\frac{x-d_1}{\sqrt{(x-d_1)^2+z^2}}\right)\end{aligned}\tag{18}$$

where all parameters on the right-hand side are known from the geometry and theory or measured from the data.

The data provided by the ultrasound scanner are in the form of I/Q data samples. A 3-D matrix of sequential frames (axial × lateral × time) is generated from the I/Q data and illustrated in Figure 3a. Because the frame rate used in sonoelastography is comparable to that in conventional Doppler ultrasound (~10 Hz), the time axis of the frame sequence is known as the slow-time axis. The spatial phase is computed from the slow-time signal for every coordinate (x, z), thereby generating a phase map for the entire scanned region of interest. An example of the slow-time signal for a location is given in Figure 3b. To compute the gradient of $\varphi(c_s, x, z)$, the phase map is unwrapped using the 1-D algorithm of MATLAB computational software (The Mathworks, Natick, MA, USA) applied in both lateral and axial dimensions. The local shear speed is then calculated for each coordinate using eqn (18) to generate the shear speed map $\hat{c}_s(x,z)$. The 2-D phase map and its unwrapped version are shown in Figure 3(c and d, respectively). As a practical matter, some spatial averaging is used to minimize the effects of noise. A 2-D median filter of 2 × 2 mm^2 is applied for each CrW frame, and a 4 × 4 mm^2 median filter is applied to the final shear speed map. This algorithm is applied to the experiments described in the next section.

EXPERIMENTS

Five experimental data sets were acquired and analyzed to validate the performance of the proposed experimental setup illustrated in Figure 1b and the

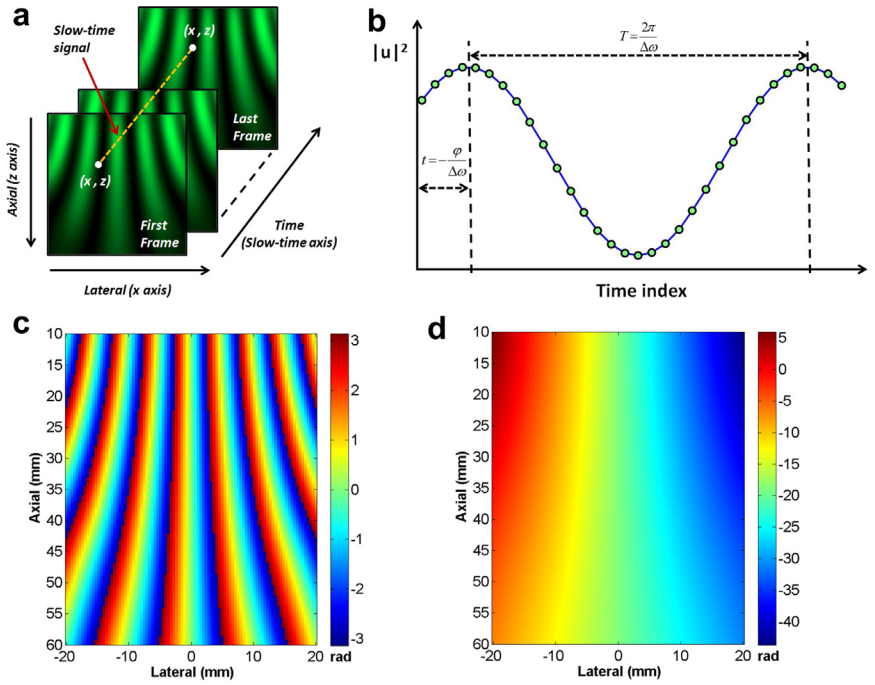

Fig. 3. (a) Three-dimensional matrix of the crawling waves (CrW). The axial, lateral and slow-time axes correspond to the depth, width and time of the CrW movie, respectively. A set of data samples through the slow-time axis for a specific coordinate is called slow-time signal (*dashed line*). (b) A slow-time signal for a location. The number of samples of a slow-time signal equals the number of frames of the movie sequence. To recover the phase φ, the slow-time signal should contain at least one sinusoidal cycle. (c, d) The phase map (c) and the unwrapped phase map (d) were computed from the simulated CrW.

estimation algorithm. Four experiments were performed on tissue-mimicking phantoms and one experiment was performed on *ex vivo* human liver under informed consent and an institutional review board-approved protocol.

Two phantoms were prepared: a homogeneous 17% gelatin phantom, and one inclusion phantom with 17% gelatin within the inclusion and 9.3% gelatin within the background. The percentages are with respect to the weights of the gelatin and water. The process for homogeneous phantom preparation is analogous to the phantom preparation procedure used in *ex vivo* prostate and liver experiments (Barry et al. 2012; Castaneda et al. 2009). The homogeneous phantom consists of 2 L degassed water, 409 g porcine gelatin (300 Bloom Pork Gelatin; Gelatin Innovations, Schiller Park, IL, USA), 19.66 g salt (sodium chloride, BDH, Conestoga, PA, USA) and 3.27 g agar (Difco Agar Technical Solidifying Agent, BD, Sparks, MD, USA). The components were mixed together and heated to a temperature of 55°C. The molten mixture was then poured into a cube-shaped mold for hardening. The inclusion phantom preparation consists of two main steps: inclusion fabrication and the embedding of the inclusion into the background phantom. In the process of inclusion fabrication, once the mixture had been heated to 55°C, the solution was poured into a cylindrical mold (approximately 10 mm in diameter) and placed in a refrigerator (approximately 5°C) for hardening. Once solidified, the inclusion was placed into a cube-shaped box. The water-gelatin mixture of the background material (2400 mL degassed water, 246 g gelatin, 3.6 g agar, 21.6 g salt) was heated to 55°C and then cooled to 32°C before being poured into the box. Because the inclusion and the background are 17% and 9.3% gelatin, respectively, the inclusion is stiffer than the background.

The prepared phantoms were scanned in three different cross sections. A single cross section in the 17% gelatin phantom was scanned using the setup shown in Figure 1b. The cylinder phantom was scanned in two cross sections, as outlined in Figure 4. A homogeneous section (9.3% gelatin) in the cylinder phantom (dotted outline in Fig. 4) was scanned using setups illustrated in Figure 1a (sources labeled *I*) and Figure 1b for comparison. The vibration frequencies of the sources were 250 and 250.4 Hz. Finally, a cross section that includes the cylinder (dashed outline in Fig. 4) was scanned using the proposed setup with vibration frequencies of 220 and 220.4 Hz. In all phantom experiments, the temperature of the phantoms was approximately 19°C (room temperature). In addition to the phantom

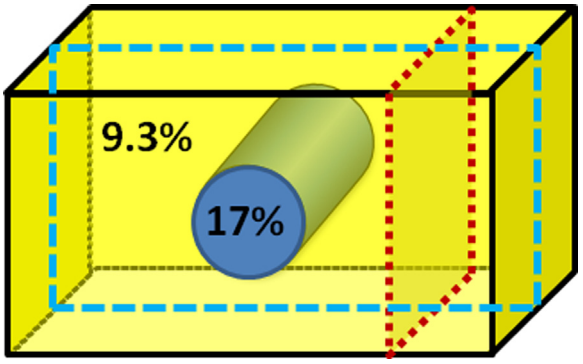

Fig. 4. The cylinder phantom was scanned in two different cross sections: a homogeneous section (*dotted line*) and a section that includes both the cylinder and the background (*dashed line*).

experiments, a whole human liver was scanned using the same setup (Fig. 1b). The liver was provided for the experiment after hepatectomy, under approved consent. The sources, vibrating at 90 and 90.45 Hz, excited the liver through a gelatin layer that operated as a standoff pad. Note that different vibration frequencies were used in liver and phantom experiments. The choice of frequency range depends on the shear wave attenuation, α_s, and the sample size of the biomaterial. The far-field distance in all experiments (according to a^2/λ_s) starts at a distance less than 1 cm.

In each experiment, a dual-channel signal generator (AFG3022 B, Tektronix, Beaverton, OR, USA) produces two sinusoidal signals with a slight difference between the frequencies, $\Delta\omega$. To generate a slowly propagating shear wave interference pattern (CrW), the frequency difference is set in the range 0.3–0.5 Hz. Each output signal from the function generator passes through a digital power amplifier (Model LP-2020 A+, Lepai, Bukang, China) and is then supplied to a miniature vibration source (Model NCM02–05–005–4 JB, H2 W, Linear Actuator, Santa Clara, CA, USA). The vibration sources are placed on top of the biomaterial and vibrate in a direction that is normal to the surface of the medium (z axis in accordance with Fig. 2a). A linear array ultrasound transducer (M12 L, GE Healthcare, Milwaukee, WI, USA) is positioned between the vibration sources and scans the medium. The sonoelastography imaging mode displays the CrW on the ultrasound display (Logiq 9, GE Healthcare).

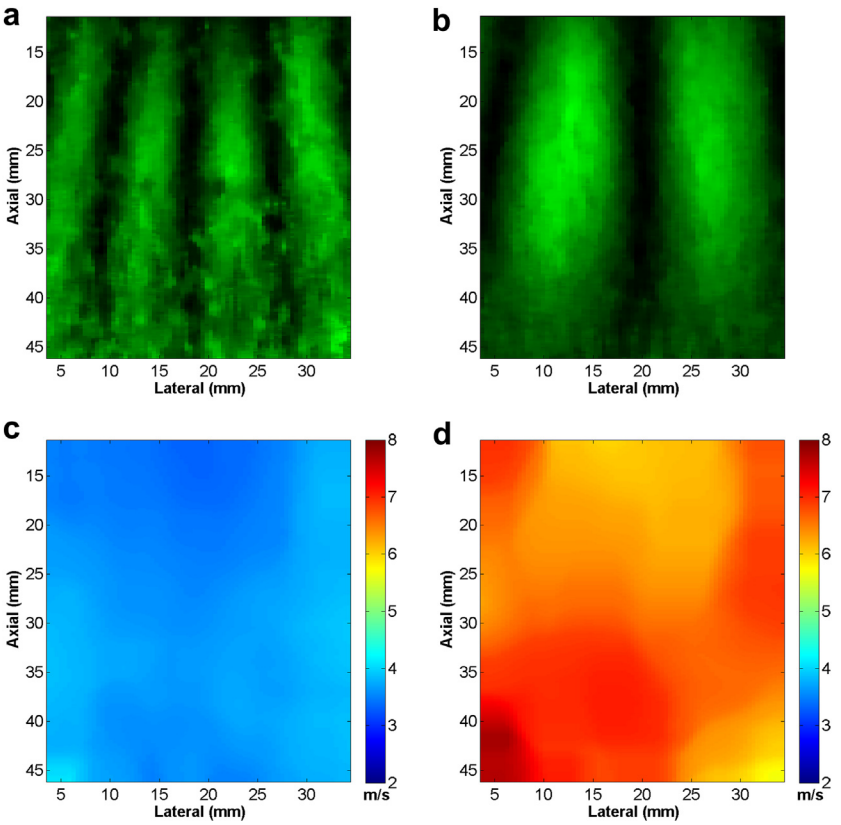

Fig. 5. Homogeneous phantom experiments. (a, b) Crawling waves movie frames of the 9.3% phantom (a) and 17% phantom (b). (c, d) The shear speed maps of the 9.3% and 17% phantoms, respectively. In both experiments the vibration frequency and the vibration frequency offset are 250 and 0.4 Hz, respectively.

A DICOM (Digital Imaging and Communications in Medicine) file is saved for each experiment and transferred to a personal computer (PC) for processing.

The estimated average shear speeds of the 9.3% and 17% homogeneous cross sections are 3.66 ± 0.3 and 6.63 ± 0.5 m/s, respectively, calculated over a region of interest of 35 × 30 mm^2, centered at a depth of 30 mm. This verifies that the 17% phantom is stiffer than the 9.3% phantom. A single frame of each CrW movie and the corresponding shear speed maps are illustrated in Figure 5. The bright and dark stripes (green and black color schemes, respectively, in color Doppler) indicate regions of high and low displacement amplitudes, respectively. The distance between the stripes is proportional to the shear speed. As both phantoms were scanned with the same vibration frequencies, it is evident from Figure 5 that the 17% phantom has higher shear speed than the 9.3% phantom (fewer stripes indicate higher shear speed). The shear speed value obtained for the 9.3% homogeneous section using the elongated bars is 3.5 ± 0.1 m/s over a region of interest of 35 × 30 mm^2. This value correlates with the estimated shear speed (3.66 m/s) for the same cross section obtained with the circular sources setup. In addition, mechanical measurement using a stress relaxation test, as described by Zhang et al. (2007), was previously applied to a 9.3% phantom and exhibited a shear speed value of 3.6 m/s, which also correlates with the estimated shear speed in this study.

For the inclusion experiment, the B-scan, a CrW movie frame, the unwrapped phase map and the shear speed map are illustrated in Figure 6. The average shear speeds within the inclusion and the background are 5.34 ± 0.35 and 3.7 ± 0.4 m/s, respectively. The shear speed value of the background correlates with the estimated shear speed from the experiment performed on the homogeneous cross section of the same phantom. However, the estimated shear speeds within the 17% inclusion and 17% homogeneous phantom differ. This may stem from the general rule that to detect a structure in a medium, the wavelength should be larger than the dimension of the target structure. This condition is not satisfied because the inclusion diameter is approximately

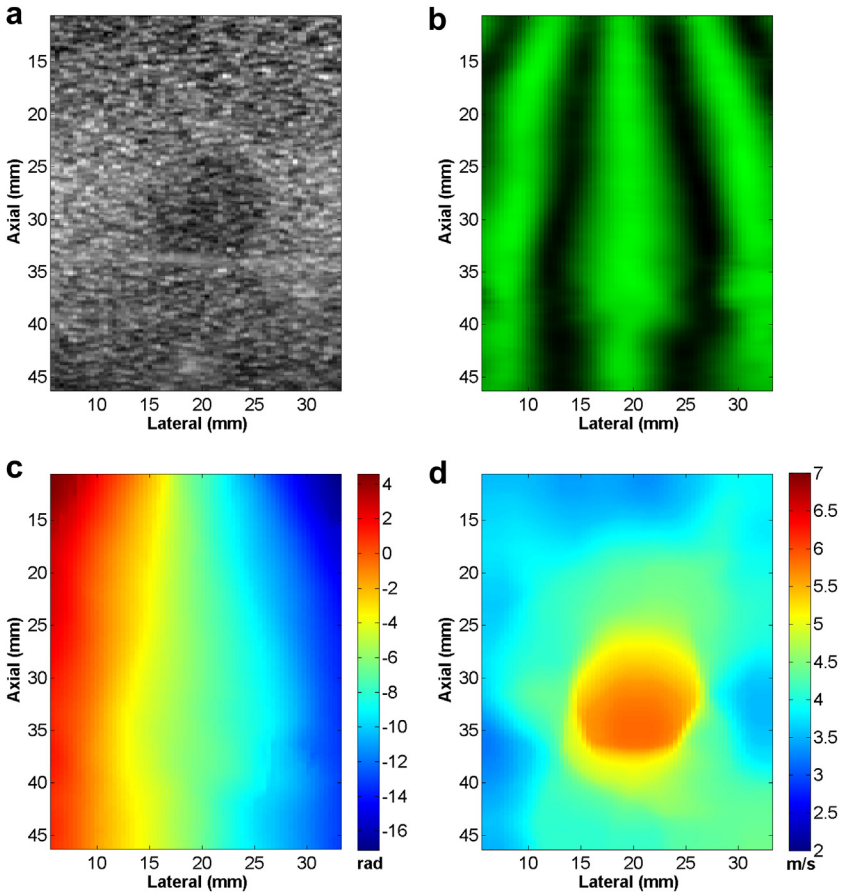

Fig. 6. Inclusion phantom experiment. The inclusion is 17% gelatin, and the background is 9.3% gelatin. The vibration frequency and vibration frequency offset are 220 and 0.4 Hz, respectively. (a) B-Scan of the phantom. (b) Single frame of the crawling waves movie. (c) Unwrapped phase map. (d) Computed shear speed map.

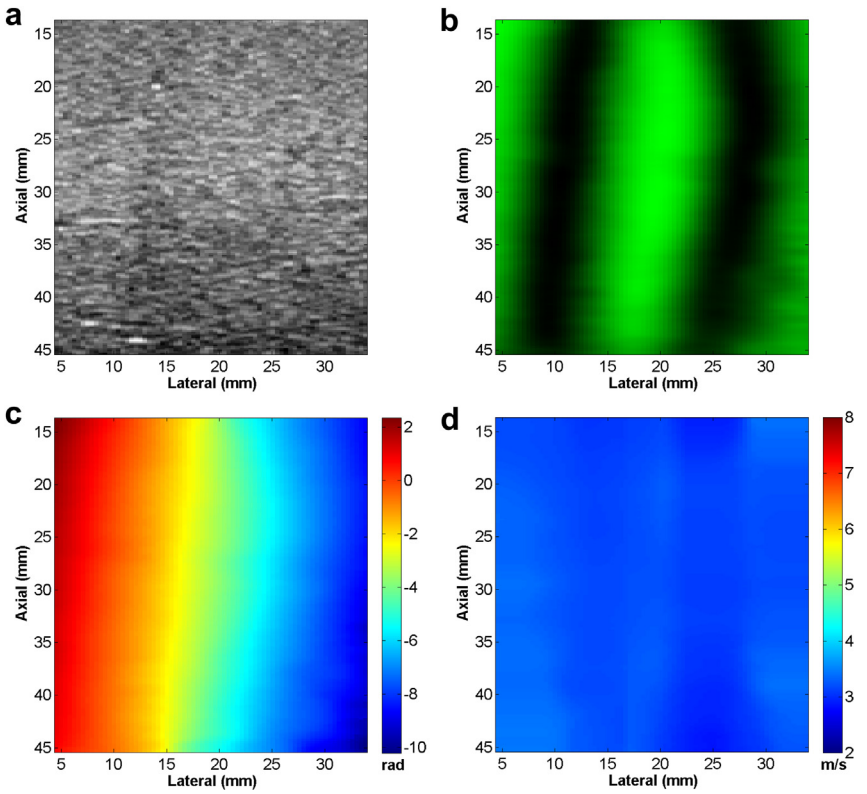

Fig. 7. *Ex vivo* human liver. The vibration frequency and vibration frequency offset are 90 and 0.45 Hz, respectively. (a) B-Scan of the liver. (b) Single frame of the crawling waves movie. (c) Unwrapped phase map. (d) Shear speed map.

10 mm and the wavelength is about 30 mm (assuming that c_s = 6.5 m/s and given that the vibration frequency is 220 Hz). Although the estimated shear speed within the inclusion may be underestimated, the inclusion can be revealed on the shear speed map, as illustrated in Figure 6d.

The liver was recovered from a previously healthy patient who died of a ruptured cerebral aneurysm. All liver biochemical tests were normal, and liver biopsy revealed less than 5% steatosis (fat concentration). Consent for research was obtained from the patient's family before recovery. The liver was not used for transplant because of logistical issues resulting in a prolonged cold ischemia time. After hepatectomy, the liver was placed in a plastic bag filled with a preservative solution and refrigerated for approximately 48 h before scanning. Liver images including the B-scan, a CrW movie frame, the unwrapped phase map and the computed shear speed map are given in Figure 7. The estimated average shear speed within the liver is 3 $\pm$ 0.1 m/s over a region of interest of 35 $\times$ 30 mm^2, centered at a depth of 30 mm. This value correlates with the estimated shear speed obtained by Barry et al. (2012) in an *ex vivo* human liver. *In vivo* studies (Muller et al. 2009; Sandrin et al. 2003), however, report lower shear speed values than the *ex vivo* liver studies. This difference is due to the different temperatures of the livers during scanning. Lower temperature results in increased stiffness. Therefore, shear speed estimations obtained in *ex vivo* experiments (at room temperature, approximately 19°C) are greater than the estimations obtained *in vivo* (at body temperature, approximately 37°C).

CONCLUSIONS

The configuration of two miniature vibration sources together with the ultrasound transducer can serve as an *in vivo* elasticity imaging technique for larger organs such as the liver. A detailed analysis of the displacement field generated by the vibration sources and the developed algorithm allows mapping of the elastic properties within the scanned biomaterial. This technique was capable of identifying an inclusion on the order of 10 mm in diameter. It was also found that the proposed double-source setup can produce CrW within *ex vivo* human liver, and elasticity was mapped using the developed algorithm. Some limitations of the present study include the need for testing in more complex models including the effects of additional layers and multiple inhomogeneities. However, the results indicate that this approach can be further developed to become a handheld ultrasound-based device for elasticity mapping within soft tissues.

Acknowledgments—This work was supported by NIH Grant 5 R01 AG02980–04. The authors thank the University of Rochester Department of Electrical & Computer Engineering, and University of Rochester Medical Center departments of Transplant Surgery and Imaging Sciences.

REFERENCES

Barry CT, Mills B, Hah Z, Mooney RA, Ryan CK, Rubens DJ, Parker KJ. Shear wave dispersion measures liver steatosis. Ultrasound Med Biol 2012;38:175–182.

Blackstock DT. Fundamentals of physical acoustics. Ch. 10. New York: Wiley; 2000.

Castaneda B, An L, Wu S, Baxter LL, Yao JL, Joseph JV, Hoyt K, Strang J, Rubens DJ, Parker KJ. Prostate cancer detection using crawling wave sonoelastography. Proc SPIE 2009;7265:7265131.

Catheline S, Wu F, Fink M. A solution to diffraction biases in sonoelasticity: The acoustic impulse technique. J Acoust Soc Am 1999;105: 2941–2950.

Chen S, Kinnick RR, Greenleaf JF, Fatemi M. Harmonic vibro-acoustography. IEEE Trans Ultrason Ferroelectr Freq Control 2007;54: 1346–1351.

Fatemi M, Greenleaf JF. Ultrasound-stimulated vibro-acoustic spectrography. Science 1998;280:82–85.

Gao L, Parker KJ, Lerner RM, Levinson SF. Imaging of the elastic properties of tissue: A review. Ultrasound Med Biol 1996;22:959–977.

Garra BS. Imaging and estimation of tissue elasticity by ultrasound. Ultrasound Q 2007;23:255–268.

Greenleaf JF, Fatemi M, Insana M. Selected methods for imaging elastic properties of biological tissues. Annu Rev Biomed Eng 2003;5: 57–78.

Hah Z, Hazard C, Mills B, Barry C, Rubens D, Parker K. Integration of crawling waves in an ultrasound imaging system: Part 2. Signal processing and applications. Ultrasound Med Biol 2012;38:312–323.

Hoyt K, Castaneda B, Parker KJ. Two-dimensional sonoelastographic shear velocity imaging. Ultrasound Med Biol 2008a;34:276–288.

Hoyt K, Castaneda B, Zhang M, Nigwekar P, di Sant'agnese PA, Joseph JV, Strang J, Rubens DJ, Parker KJ. Tissue elasticity properties as biomarkers for prostate cancer. Cancer Biomark 2008b;4: 213–225.

Hoyt K, Kneezel T, Castaneda B, Parker KJ. Quantitative sonoelastography for the in vivo assessment of skeletal muscle viscoelasticity. Phys Med Biol 2008c;53:4063–4080.

Huang SR, Lerner RM, Parker KJ. On estimating the amplitude of harmonic vibration from the Doppler spectrum of reflected signals. J Acoust Soc Am 1990;88:2702–2712.

Kasai C, Namekawa K, Koyano A, Omoto R. Real-time two-dimensional blood-flow imaging using an auto-correlation technique. IEEE Trans Son Ultrason 1985;32:458–464.

Konofagou EE, Hynynen K. Localized harmonic motion imaging: Theory, simulations and experiments. Ultrasound Med Biol 2003; 29:1405–1413.

Krouskop TA, Dougherty DR, Vinson FS. A pulsed Doppler ultrasonic system for making noninvasive measurements of the mechanical properties of soft tissue. J Rehabil Res Dev 1987;24:1–8.

Lerner RM, Huang SR, Parker KJ. "Sonoelasticity" images derived from ultrasound signals in mechanically vibrated tissues. Ultrasound Med Biol 1990;16:231–239.

Lerner RM, Parker KJ. Sonoelasticity images derived from ultrasound signals in mechanically vibrated targets. In: Proceedings, Seventh European Communities Workshop, 1987.

Lerner RM, Parker KJ, Holen J, Gramiak R, Waag RC. Sonoelasticity: Medical elasticity images derived from ultrasound signals in mechanically vibrated targets. Acoust Imaging 1988;16:317–327.

McAleavey S, Menon M. 7B-3 Direct estimation of shear modulus using spatially modulated acoustic radiation force impulses. In: Proceedings, 2007 IEEE Ultrasonics Symposium, New York, 28–31 October 2007:558–561.

Miller GF, Pursey H. The field and radiation impedance of mechanical radiators on the free surface of semi-infinite isotropic solid. Proc R Soc Lond A 1954;223:521–541.

Muller M, Gennisson JL, Deffieux T, Tanter M, Fink M. Quantitative viscoelasticity mapping of human liver using supersonic shear imaging: Preliminary in vivo feasibility study. Ultrasound Med Biol 2009;35:219–229.

Nightingale K, Nightingale R, Palmeri M, Trahey G. Finite element analysis of radiation force induced tissue motion with experimental validation. In: Proceedings, 1999 IEEE Ultrasonics Symposium, Lake Tahoe, NV, 17–20 October 1999:vol. 2, pp. 1319–1323.

Nightingale KR, Palmeri ML, Nightingale RW, Trahey GE. On the feasibility of remote palpation using acoustic radiation force. J Acoust Soc Am 2001;110:625–634.

Ophir J, Alam SK, Garra B, Kallel F, Konofagou E, Krouskop T, Varghese T. Elastography: ultrasonic estimation and imaging of the elastic properties of tissues. Proc Inst Mech Eng H 1999;213: 203–233.

Ophir J, Cespedes I, Ponnekanti H, Yazdi Y, Li X. Elastography: A quantitative method for imaging the elasticity of biological tissues. Ultrason Imaging 1991;13:111–134.

Parker KJ, Doyley MM, Rubens DJ. Imaging the elastic properties of tissue: The 20 year perspective. Phys Med Biol 2011;56:R1–R29.

Parker KJ, Taylor LS, Gracewski S, Rubens DJ. A unified view of imaging the elastic properties of tissue. J Acoust Soc Am 2005; 117:2705–2712.

Sandrin L, Fourquet B, Hasquenoph JM, Yon S, Fournier C, Mal F, Christidis C, Ziol M, Poulet B, Kazemi F, Beaugrand M, Palau R. Transient elastography: A new noninvasive method for assessment of hepatic fibrosis. Ultrasound Med Biol 2003;29:1705–1713.

Sarvazyan AP, Rudenko OV, Swanson SD, Fowlkes JB, Emelianov SY. Shear wave elasticity imaging: A new ultrasonic technology of medical diagnostics. Ultrasound Med Biol 1998;24:1419–1435.

Sarvazyan AP, Skovoroda AR, Emelianov SY, Fowlkes JB, Pipe JG, Adler RS, Buxton RB, Carson PL. Biophysical bases of elasticity imaging. Acoust Imaging 1995;21:223–240.

Taylor LS, Porter BC, Rubens DJ, Parker KJ. Three-dimensional sonoelastography: Principles and practices. Phys Med Biol 2000;45: 1477–1494.

Wu Z, Taylor LS, Rubens DJ, Parker KJ. Sonoelastographic imaging of interference patterns for estimation of the shear velocity of homogeneous biomaterials. Phys Med Biol 2004;49:911–922.

Yamakoshi Y, Sato J, Sato T. Ultrasonic imaging of internal vibration of soft tissue under forced vibration. IEEE Trans Ultrason Ferroelectr Freq Control 1990;37:45–53.

Zhang M, Castaneda B, Wu Z, Nigwekar P, Joseph JV, Rubens DJ, Parker KJ. Congruence of imaging estimators and mechanical measurements of viscoelastic properties of soft tissues. Ultrasound Med Biol 2007;33:1617–1631.